Journal of Materials Chemistry B

ROYAL SOCIETY OF CHEMISTRY

PAPER

View Article Online
View Journal | View Issue

Cite this: J. Mater. Chem. B, 2023, 11, 11519

All-in-one HN@Cu-MOF nanoparticles with enhanced reactive oxygen species generation and GSH depletion for effective tumor treatment†

Shuhui Chen,‡[a] Yu Yan,‡[a] Yixuan Chen,[a] Kaili Wang,[a] Yawen Zhang,[a] Xinlong Wang,[a] Xurui Li,[a] Jian Wen *[b] and Yue Yuan *[a]

Received 17th October 2023,
Accepted 15th November 2023

DOI: 10.1039/d3tb02433d

rsc.li/materials-b

Non-invasive cancer therapies, especially those based on reactive oxygen species, including photodynamic therapy (PDT), have gained much interest. As emerging photodynamic nanocarriers, metal–organic frameworks (MOFs) based on porphyrin can release reactive oxygen species (ROS) to destroy cancer cells. However, due to the inefficient production of ROS by photosensitizers and the over-expression of glutathione (GSH) in the tumor microenvironment (TME), their therapeutic effect is not satisfactory. Therefore, herein, we developed a multi-functional nanoparticle, HN@Cu-MOF, to enhance the efficacy of PDT. We combined chemical dynamic therapy (CDT) and nitric oxide (NO) therapy by initiating sensitization to PDT and cell apoptosis in the treatment of tumors. The Cu^{2+}-doped MOF reacted with GSH to form Cu^{+}, exhibiting a strong CDT ability to generate hydroxyl radicals (•OH). The Cu-MOF was coated with HN, which is hyaluronic acid (HA) modified by a nitric oxide donor. HN can target tumor cells over-expressing the CD44 receptor and consume GSH in the cells to release NO. Both cell experiments and *in vivo* experiments showed an excellent tumor inhibitory effect upon the treatment. Overall, the HN@Cu-MOF nanoparticle-integrated NO gas therapy and CDT with PDT led to a significant enhancement in GSH consumption and a remarkable elevation in ROS production.

1. Introduction

Photodynamic therapy (PDT) is based on the energy-specific photoactivation of photosensitizers.[1] Reactive oxygen species (ROS) are produced when photosensitizers, which are activated by a certain wavelength of light, transfer energy to oxygen molecules.[2] ROS can induce cellular damage, the destruction of microvessels, and the induction of inflammation to exert anti-tumor effects.[3,4] Compared with traditional cancer treatments, such as surgery, radiotherapy, and chemotherapy, PDT has been increasingly researched and developed in the application of tumor therapy due to its low toxicity and high therapeutic specificity.[5–8] The current clinical application of PDT is mainly focused on the treatment of superficial tumors, such as skin cancer, esophageal cancer, cervical cancer, lung cancer, and other malignant neoplasms.[9–11] The efficacy of conventional PDT depends on photosensitizers, O_2, and laser irradiation. However, most photosensitizers, such as porphyrins and porphyrin derivatives have a poor water solubility and insufficient tumor accumulation, which impedes the drug delivery to cancerous cells and thus reduces their ROS production efficiency.[12] Considering this, many studies focus on drug nanocarriers for encapsulating hydrophobic drugs to address the above-mentioned issues.[8,13,14] In addition, the effect of PDT is also dramatically weakened by the overproduction of glutathione (GSH) and limited oxygen contents in the tumor microenvironment (TME).[15,16]

As a novel nano-photosensitizer, metal–organic frameworks (MOFs) are synthesized *via* the self-assembly of metal ions and organic ligands.[17] The advantages of MOFs include adjustable skeleton functional groups and pore size, high surface area, and facile surface modification. The photodynamic effect can be exerted when photosensitizers are used as organic ligands in MOFs, which not only retains the PDT efficacy of photosensitizers, but also simultaneously and effectively resolves the instability of photosensitizers due to their and significant self-aggregation.[18,19] According to previous studies, the benefit of using porphyrin MOFs for PDT is their long-term ordered structure, which not only preserves the PDT efficacy of

[a] School of Pharmacy, Shenyang Key Laboratory of Functional Drug Carrier Materials, Shenyang Pharmaceutical University, 103 Wenhua Road, Shenyang, 110016, P. R. China. E-mail: hiyueyuan@163.com; Tel: +86-24-43520585
[b] Department of Breast Surgery, The Fourth Affiliated Hospital of China Medical University, No. 4 Chongshan East Road, Shenyang, Liaoning, 110032, P. R. China. E-mail: wenjian@cmu.edu.cn; Tel: +86-24-62043436

† Electronic supplementary information (ESI) available. See DOI: https://doi.org/10.1039/d3tb02433d

‡ Shuhui Chen and Yu Yan contribute equally to this work.

porphyrins but also successfully prevents porphyrins from self-aggregating.[20] These unique properties make MOFs a promising potential drug carrier. However, due to the special microenvironment of tumor cells under hypoxia and high concentration of GSH, single PDT is not sufficient to inhibit tumor growth.[21] Therefore, identifying a strategy to deplete the elevated levels of GSH in cancer cells and alleviate their hypoxic microenvironment for enhancing the therapeutic efficacy of PDT against tumors is an important research direction.

Chemodynamic therapy (CDT) is a cancer treatment method that catalyzes the conversion of hydrogen peroxide (H_2O_2) into hydroxyl radicals ($^{\bullet}OH$) *via* Fenton or Fenton-like reactions.[14,22] In this therapy, the reaction solely occurs with the overproduced H_2O_2 in tumor cells, thereby conferring CDT with low side effects and high selectivity.[23] Copper is an essential element for human health. Studies have shown that the safe intake of copper in adults is as high as 10 mg per day.[24] Accordingly, Cu^{2+} is a frequently applied transition metal in CDT, which can consume the extra GSH generated by tumor cells to produce Cu^{+}, thus carrying out a Fenton-like reaction, increasing oxidative stress in cells and decreasing the clearance of $^{\bullet}OH$.[25–28] In addition, Cu^{2+} is easily oxidized into Cu^{+} in the weakly acidic TEM, which can be approximately 160-times faster than that of Fe^{2+}.[29,30] Inspired by this, Cu^{2+}-doped MOFs have been designed.

To enhance the therapeutic efficacy of PDT against tumors, it is crucial to employ certain means that can alleviate the hypoxic tumor microenvironment. Nitric oxide (NO), a common gas mediator, is involved in apoptosis, angiogenesis, and immunological responses. Furthermore, NO can be utilized to improve anticancer effects and reverse drug resistance to several medications.[13,31,32] Numerous studies have shown that low levels of NO (pM–nM) exhibit anti-apoptotic effects and stimulate angiogenesis, which aid in the formation of tumors. In contrast, high levels of NO (μM concentration) may directly or indirectly show a cytotoxic effect, leading to DNA-based deamination, cell function damage, inhibition of mitochondrial respiration, and finally cell apoptosis.[33] Additionally, elevated NO levels can treat tissue hypoxia by relaxing blood vessels. In recent years, an increasing number of studies has focused on NO donors. Nitric ester-based NO donors could catalyze the GSH/GSSG redox process, leading to the depletion of intracellular tumor GSH and production of NO.[34,35] Consequently, the level of oxidative stress in tumor cells increased, which may contribute to the sensitization of PDT.[36–38]

The attainment of a favorable tumor treatment outcome necessitates the presence of an effective targeting effect. CD44 is a transmembrane cell surface glycoprotein. Although its endogenous expression in normal tissues is at a low level, it is highly expressed in various types of tumor cells such as breast cancer,[39] lung cancer,[40] and hepatocellular carcinoma.[41] HA, also referred to as glucuronic acid, exhibits affinity for the CD44 receptor and can be used as a targeting ligand for tumors.[42] The N-terminus of CD44 demonstrates selective binding to HA, thereby making it possible for HA and its derivatives to actively target tumor tissues that overexpress the CD44 receptor.[43] The utilization of HA as a drug carrier confers the benefit of enhancing drug solubility, stability, and bioavailability, while simultaneously exhibiting active tumor targeting. Furthermore, due to the presence of free hydroxyl and carboxyl groups in the structure of HA, it can be conjugated with other functional substances *via* chemical or hydrogen bonding.[44]

Herein, this study focused on the limited efficacy of PDT and designed a novel nanostructure (HN@Cu-MOF) to achieve a synergistic PDT/CDT/GT effect. As shows in Scheme 1, firstly, a Zr-based MOF was prepared, and then a Cu-MOF (Cu^{2+}-doped MOF) was synthesized utilizing a simple ion doping technique. To specifically bind to the highly expressed CD44 receptors on the surface of cancer cells and enable nitric oxide (NO) release

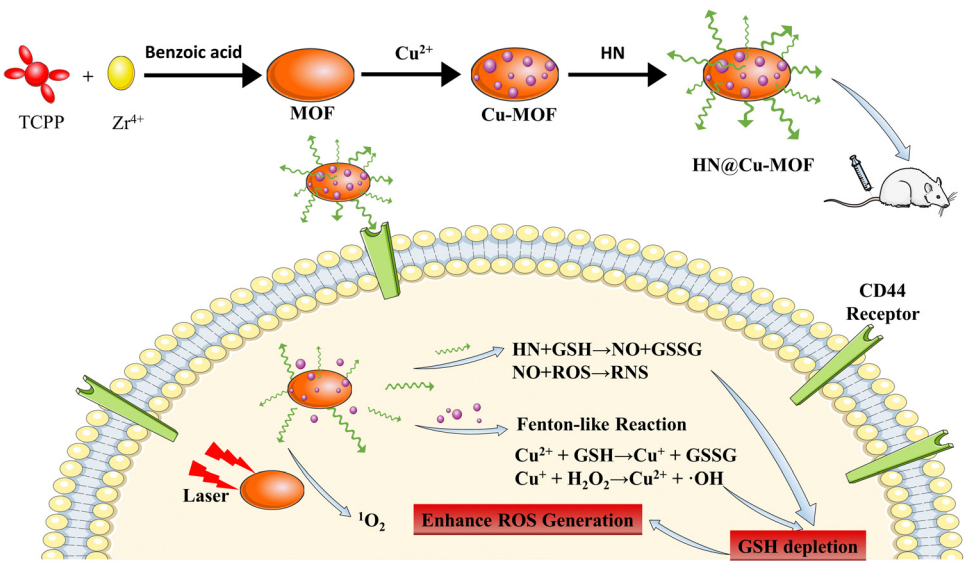

Scheme 1 The fabrication procedure of the HN@Cu-MOF and a schematic of its therapeutic mechanism for PDT, CDT, and NO gas therapy.

triggered by GSH, the Cu-MOF was electrostatically adsorbed on nitric oxide donor-modified hyaluronic acid (HN). Upon activation by a 655 nm laser, the Cu^{2+} in HN@Cu-MOF reacted with the excessive GSH in tumor cells, thereby reducing the antioxidant capacity of tumor cells, enhancing singlet oxygen oxygen-mediated cytotoxicity and producing Cu^{+}.[45] Simultaneously, HN can also release NO by depleting GSH, while alleviating the oxygen-poor environment of tumors, thus further promoting the role of PDT (Scheme 1).[31] Additionally, the *in vivo* experiments showed that HN@Cu-MOF NPs had a fantastic anti-tumor impact.

2. Experimental

2.1. Chemicals and materials

Pyrrole, sodium hyaluronate (M_W = 6 kDa) were obtained from Macklin Co., Ltd. HAase and HA were obtained from Innochem Technology Co., Ltd. Tetrakis(4-carboxyphenyl)porphyrin (TCPP) was purchased from Innochem Technology Co., Ltd. (Beijing, China). Methyl 4-formylbenzoate, benzoic acid, $ZrOCl_2{\cdot}8H_2O$, and zirconyl chloride octahydrate were acquired from Aladdin Biochemical Technology Co., Ltd. Reduced GSH, copper chloride hexahydrate ($CuCl_2{\cdot}2H_2O$), methylene blue (MB) and H_2O_2 were purchased from Aladdin Reagents (Shanghai, China). 2,7-Dichlorodihydrofluorescein diacetate (DCFH-DA), Griess Reagent Assay kit and diaminofluorescein-FM diacetate (DAF-FM DA) were acquired from Beyotime Biotechnology (Shanghai, China). Fetal bovine serum, Dulbecco's modified Eagle medium (DMEM), phosphate-buffered saline, trypsin, penicillin–streptomycin, 3-(4,5-dimethyl-2-thiazolyl)-2,5-diphenyl-2*H*-tetrazolium bromide (MTT), and 4′,6-diamidino-2-phenylindole (DAPI) were purchased from Dalian Meilun Biotechnology Co., Ltd. The Kunming female mice (18–20 g) used in the experiment were purchased from Changchun Changsheng Biotechnology Co., Ltd. The guidelines set by the National Regulation of China for the Care and Use of Laboratory Animals were followed in all *in vivo* research.

2.2. Synthesis of MOF

The MOF was synthesized based on previous studies.[46] The steps in the experiment are as follows. Briefly, TCPP (10 mg), $ZrOCl_2{\cdot}6H_2O$ (30 mg), and benzoic acid (280 mg) were dissolved in 10 mL *N*-dimethylformamide (DMF). Then, the mixture was heated for 5 h at 90 °C. After centrifugation, the MOF was collected and washed with DMF. The MOF was obtained after vacuum drying.

2.3. Synthesis of Cu-MOF

Firstly, the MOF (20 mg) was dispersed evenly in DMF (20 mL) under ultrasonication. Then, $CuCl_2{\cdot}2H_2O$ (40 mg) and the MOF were stirred for 12 h at 100 °C to obtain the Cu^{2+}-doped MOF. The Cu-MOF was separated after centrifugation and washed with DMF and DI water separately. Then, the Cu-MOF was redispersed in DI water and refrigerated at 4 °C.

2.4. Synthesis of HN

HN was synthesized based on previous reports.[34] Briefly, silver nitrate (3.7 g) was reacted with bromoacetic acid (2 g) in anhydrous acetonitrile (80 mL) at 70 °C for 12 h. Following filtration, the product was repeatedly filtered with dichloromethane (100 mL) to remove silver bromide and silver nitrate. After several rounds of purification, dichloromethane was extracted through vacuo to produce 2-(nitrooxy)acetic acid, a yellow oil. To activate the carboxyl groups, 2-(nitrooxy) acetic acid (40 μL), DMAP (28 mg), EDC (240 mg), and NHS (144 mg) were dissolved in 12 mL of phosphate buffer (pH 6.0) and agitated for 1.5 h at room temperature. After activation, the pH was set to 8 and HA (58 mg) added, and the mixture stirred for 24 h. Then, the mixture was filtered through 48 h of dialysis and concentrated in an ultrafiltration centrifuge tube (10 K MWCO) (Millipore), reduced to 2 mL, and kept at 4 °C.

2.5. Synthesis of HN@Cu-MOF

Briefly, 70 μL HN and Cu-MOF (2 mg) was dissolved in 20 mL DI water and kept stirring for 5 min. Then, to remove the unloaded HN, the HN-coated Cu-MOF was centrifugated and washed by DI water. Then, HN@Cu-MOF was redispersed in DI water and stored at 4 °C.

2.6. Characterization

The construction of the 2-(nitrooxy) acetic was confirmed by nuclear magnetic resonance spectroscopy. The combination of HA and 2-(nitrooxy) acetic nuclear was analyzed *via* Fourier transform infrared (FTIR) spectroscopy in the spectral range of 400–4000 cm^{-1}. The particle size of the MOF, Cu-MOF, and HN@Cu-MOF was investigated using a dynamic light scattering (DLS) analyzer (Zetasizer 3000 HAS, Malvern, UK). The successful synthesis of the MOF and Cu^{2+} doping were verified by X-ray powder diffraction (SmartLab-SE, Japan) and energy disperse spectroscopy. Scanning electron microscopy (SEM) and transmission electron microscopy (TEM) were used to study the morphology of Cu-MOF and HN@Cu-MOF. According to TEM imaging, a layer had developed on the surface of the Cu-MOF, proving the successful coating of HN on Cu-MOF.

2.7. Stability tests of HN@Cu-MOF

To assess the stability of HN@Cu-MOF in PBS (pH 7.4) or 10% FBS culture medium at 25 °C, we recorded its particle size and polydispersity index (PDI) at various intervals (0, 1, 2, 4, 6 and 8 days).

2.8. GSH depletion

HN@Cu-MOF and GSH (0, 1, 2, 4, 6 mM) were incubated at 37 °C for 4 h. After centrifugation, DTNB (0.2 mM) was added to the supernatant and incubated at 37 °C for 3 min. The absorbance of the solution was recorded at a wavelength in the range of 370–500 nm during each interval.

2.9. GSH-responsive NO release

The Griess reagent kit was employed to quantify the GSH-enhanced NO release of HN@Cu-MOF. In response to GSH, the HN@Cu-MOF-released NO was converted to nitrite and reacted with the Griess reagent to fabricate diazo compounds, which could be observed under UV light at 540 nm. A microplate reader was used to assess the absorbance after 50 μL of medium was collected at various intervals (0, 15, 30, 45, 60, 90, 105, 150, 210, and 270 min) and subjected to the Griess reagent reaction. The concentration of NO in the sample was calculated according to the NO standard curve.

2.10. Detection of hydroxyl radical ($^{\bullet}$OH) release

Methylene blue (MB) was used for the detection of $^{\bullet}$OH. HN@Cu-MOF, MB, GSH (10 mM), H_2O_2 (10 μM), and HAase were divided into different experimental groups and incubated for various intervals (0, 1, 2, 3, 4, and 5 min) at 37 °C. After centrifugation, the UV-vis spectrum of the obtained supernatant at 664 nm was recorded.

2.11. Detection of $^1O_2$

The steps of the experiment are as follows. Briefly, 1,3-diphenylisobenzofuran (DPBF) and HN@Cu-MOF were added to dimethyl sulfoxide (DMSO) and either placed in ambient light or exposed to 655 nm laser irradiation (50 mW cm^{-2}, the laser source was roughly 1 cm away) at various intervals (0, 2, 4, 6, 8, and 10 min). After laser irradiation, the UV-vis absorbance at 417 nm was recorded.

2.12. Cell culture

Murine breast cancer 4T1 cells were cultured in Dulbecco's modified Eagle medium (DMEM) supplemented with approximately 10% fetal bovine serum (FBS) and 1% antibiotics (streptomycin and penicillin) in an environment of 37 °C and 5% CO_2.

2.13. Cytotoxicity assay

The MTT assay was used to determine the cytotoxicity of the MOF, Cu-MOF, HA@Cu-MOF, and HN@Cu-MOF with or without laser irradiation. The cells were cultured in 96-well plates (1.0×10^4 cells per well) and incubated for 12 h for adherent growth. After removing the medium, the cells were incubated with 200 μL of MOF, Cu-MOF, HA@Cu-MOF or Cu-MOF at several concentrations overnight. Then, the cells were irradiated (655 nm, 50 mW cm^{-2}) for 3 min. After, they were incubated for an additional 12 h to measure the cytotoxicity caused by laser irradiation. The cells that were not exposed to radiation were used to assess the dark toxicity of the formulations. Subsequently, MTT solution (5 mg mL^{-1}) was added to a volume of 20 mL, and the liquid in each well was withdrawn after 4 h of incubation. Then, 200 μL of DMSO was added to each well to dissolve the formazan, which was used to determine the vitality of the cells by measuring the absorbance at 490 nm.

2.14. Cellular uptake

The cellular uptake of HN@Cu-MOF was analyzed as follows. Briefly, 4T1 cells (1×10^4 cells per well) were incubated in 6-well plates for 24 h, and then incubated until they adhered to the cell wall. To examine the cellular uptake of MOF, Cu-MOF and HN@Cu-MOF, the cells were cultured for 4 h with the same concentrations of NPs. In particular, to confirm the targeting role of HN, certain wells containing 4T1 cells were pre-incubated with free HN (1 mg mL^{-1}, 500 μL) for 1 h to saturate the CD44 receptor. After cleaning, the cells were stained with DAPI for 5 min. Confocal laser scanning microscopy (CLSM) was used to take pictures of the fixed cells to analyze the cellular uptake activity.

2.15. Cellular ROS analysis

DCFH-DA is a common probe to study the intracellular ROS levels *via* CLSM. 4T1 cells were seeded in a 6-well plate (1×10^4 cells per well) and incubated for 12 h. After incubation with MOF, Cu-MOF and HN@Cu-MOF at the same concentration, the cells were incubated for another 24 h. Subsequently, the cells were treated for 30 min with a DCFH-DA solution (10 μM, 1 mL). The cells were washed twice with PBS before being subjected to 3 min of laser irradiation (655 nm, 50 mW cm^{-2}). The fluorescence intensity of CLSM was utilized to monitor the nanoparticles in the living cells.

2.16. Cellular NO release analysis

The DAF-FM DA probe was used to identify the detection of NO released in 4T1 cells. Briefly, 4T1 cells (1×10^4 cells per well) were planted in a 6-well plate and the dish was incubated for 12 h. Afterwards, the cells were incubated with Cu-MOF or HN@Cu-MOF at an equivalent dose for 12 h. The cells were washed twice with PBS before being stained for 4 h with DAF-FM DA. Subsequently, fluorescence imaging was carried out using CLMS.

2.17. Tumor model

The animal experiments were conducted with permission of the Experimental Animal Ethics Committee at Shenyang Pharmaceutical University and in accordance with the guidelines of the University's Animal Experimentation Centre. To establish 4T1 cell breast cancer-bearing models, KM mice were injected with 5×10^6 4T1 cells in their back. The status, tumor growth and body weight of the mice were observed daily. The mice were randomly divided into five groups after the tumor volume reached about 100 mm^3 to conduct an experiment.

2.18. Hemolysis tests

A hemolysis test was performed to investigate the biological safety of HN@Cu-MOF. Blood was collected from the orbital cavity of the mice and placed in centrifuge tubes pre-coated with heparin. The 2% red blood cell (RBC) suspensions and HN@Cu-MOF were mixed as indicated in the table. The mixture was incubated for 4 h at 37 °C. After centrifugation, the degree of hemolysis was analyzed by visually observing the

supernatant and compared it with the solution without HN@Cu-MOF.

2.19. Distribution of MOF complex in tumor-bearing mice

The KM mice bearing 4T1 cells breast cancer tumors were randomly divided into two groups and injected with Cu-MOF NPs or HN@Cu-MOF NPs. The tumors and major organs were removed at 4, 8, 12, 24 and 48 h, respectively. After saline cleaning, we used fluorescence imaging to observe the organs of the tumor-bearing mice and recorded their peak fluorescence intensity over time.

2.20. *In vivo* anti-tumor efficiency evaluation

The tumor volume was computed as volume = (tumor width)^2/2(tumor length). The tumors were thoroughly removed and weighed after treatment to assess the therapeutic efficacy. The tumor-bearing mice were randomly divided into 5 groups (n = 5), as follows: (1) saline group, (2) Cu-MOF group, (3) Cu-MOF + laser group, (4) HN@Cu-MOF group and (5) HN@Cu-MOF + laser group. The mice were injected every 2 days for a period of 10 days. After about 12 h of injection, the mice in groups (3) and (5) were subjected to irradiation from a 655 nm laser (200 mW cm^{-2}) for 10 min. To assess the anticancer impact, the tumor growth and weight were measured every two days with digital calipers and electronic balance. After treatment, the tumors were carefully excised and weighed to appraise the therapeutic efficacy.

2.21. Histology staining

On the eleventh day of treatment, the tumor-bearing mice were euthanized and all their vital organs and tumor tissues were soaked in formalin and paraffin. Subsequently, the tissues were sectioned for hematoxylin and eosin (H&E) staining.

2.22. Statistical analysis

All data in this research are presented as mean ± standard deviation (SD) and compared by one-way ANOVA test using the SPSS software. A p value of <0.05 was considered as statistically significant ($^*p < 0.05$, $^{**}p < 0.01$, $^{***}p < 0.001$).

3. Results and discussion

3.1. Characterization

A spherical-like MOF was synthesized according to previous reports.[46] The MOF was formed through the connection between Zr_6 clusters and the TCPP ligand. Each Zr_6 cluster is connected to 6 TCPP ligands, exposing unsaturated N atomic sites.[47] Then, Cu^{2+} was easily doped in the MOF through the formation of an N–Cu bond to form Cu-MOF to consume GSH in the TME, and the morphology was confirmed by TEM images, as shown in Fig. 1A. The XRD patterns of both MOF and Cu-MOF (Fig. 1B) showed a few strong peaks at 4.72°, 6.66°, 8.08° and 9.28°, representing the successful synthesis of MOF and Cu-MOF. After doping Cu^{2+}, the peaks of Cu-MOF declined, showing that the crystallinity of the MOF decreased, which is consistent with the previous study.[48] This is due to the chelation of Cu^{2+} in the porphyrin ring, leading to an increase in disorder in the crystal structure of the MOF. The EDS analysis of MOF and Cu-MOF (Fig. 1C and D, respectively) revealed the absence of any detectable Cu signal in the MOF, while the weight percentage of Cu in Cu-MOF was determined to be 2.37%. The FTIR spectra of TCPP, MOF and Cu-MOF are displayed in Fig. 1E and F. Compared with TCPP, both MOF and Cu-MOF showed a decrease in the vibrational absorption intensities of C=O groups at approximately 1700 cm^{-1}. This phenomenon is due to the coordination between Zr^{4+} and –COOH of TCPP in the MOF. After Cu^{2+} doping, the stretching peak of N–Cu at about 1000 cm^{-1} appeared. The appearance of the N–Cu peak certified the successful integration of Cu^{2+} in the porphyrin ring of MOF.

Hyaluronic acid (HA) reacted with 2-(nitrooxy) acetic acid *via* the catalysis of NHS, EDC and DMAP to form HN, as previously described in the literature.[34] Also, Fig. 2A and B display the precise synthetic pathways for HN. The ^{1}H-NMR spectrum of 2-(nitrooxy) acetic acid in D_2O showed a representative peak at δ 4.7 (Fig. 2C). The FTIR spectra of HA and HN are displayed in Fig. 2D and E. The spectra of HA and HN exhibit similar characteristics, indicating that the basic structure of HA remained unchanged. Compared with HA, the spectrum of HN exhibits symmetrical nitro group stretching vibration peaks at 1410 cm^{-1}, an asymmetrical nitro group stretching vibration peak at 1384 cm^{-1} and a symmetrical stretching vibration peak of O–N=O group at 1053 cm^{-1}. The appearance of these peaks confirmed the successful synthesis of HN, as demonstrated in the magnified spectra in the range of 500 to 2000 cm^{-1}.

Then, HN was electrostatically absorbed on the surface of Cu-MOF to create HN@Cu-MOF. The significant differences in size and zeta-potential between Cu-MOF and HN@Cu-MOF both indicate the successful addition of an HN shell on the exterior of Cu-MOF (Fig. 3A and B). The presence of a thin film on the surface of Cu-MOF further validated the formation of HN@Cu-MOF, as shown in the TEM image (Fig. 2F), demonstrating the successful coating with HN. HN@Cu-MOF was dispersed in water and a photo of it recorded under ambient light and UV irradiation (λ = 365 nm), as shown in Fig. S1 (ESI†). Also, HN@Cu-MOF was placed in contain-serum culture medium and PBS 7.4 at 25 °C for 8 days to evaluate its stability. Its hydrodynamic diameter and polydispersity index (PDI) remained largely unchanged for 8 days (Fig. S2, ESI† and Fig. 3C, D).

3.2. GSH consumption and NO release

5,5′-Disulfide(2-nitrobenzoic acid) (DTNB) is a commonly used probe for the determination of GSH. The colorless DTNB reacts with GSH to produce a yellow molecule, which has a maximum absorption at 412 nm. After the HN@Cu-MOF was incubated with GSH, the GSH was consumed by doped Cu^{2+}. The absorbance at 412 nm decreased gradually when HN@Cu-MOF was mixed with different concentrations of GSH, as shown in Fig. 4A. The NO release profile of HN@Cu-MOF was displayed using the typical Griess assay. Once NO merged in the solution, it underwent a Griess reaction and formed a pink azo dye with a

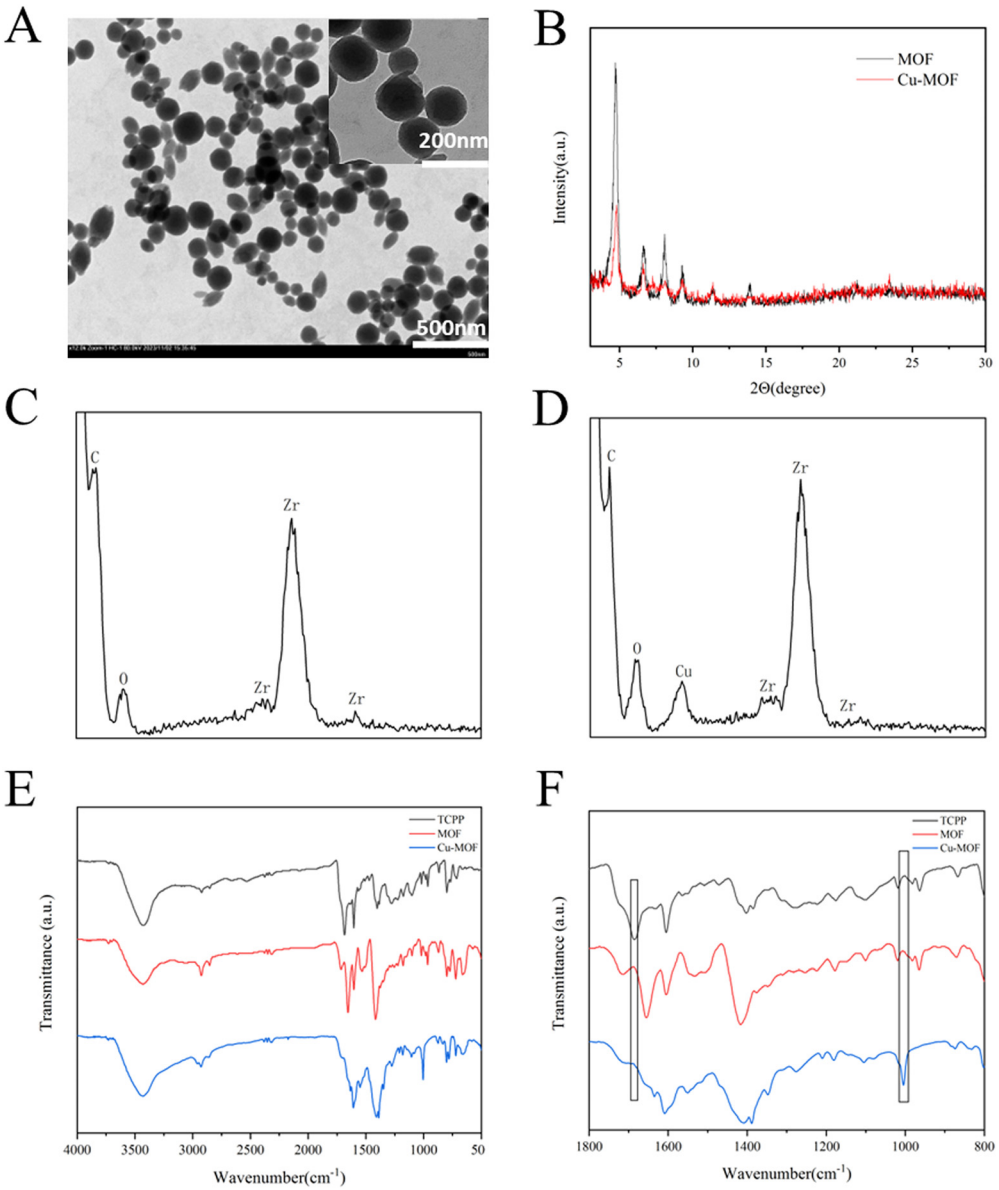

Fig. 1 (A) The TEM images of Cu-MOFs. (B) The XRD patterns of MOFs and the Cu-MOF. (C) The EDS analysis of the element composition of MOFs. (D) The EDS analysis of the element composition of the Cu-MOF. (E) The FTIR spectra of TCPP, MOFs and Cu-MOFs. (F) The magnified FTIR spectra of TCPP, MOFs and Cu-MOFs.

strong absorption at 540 nm. HN@Cu-MOF alone did not release NO and had no absorption at 540 nm. On the contrary, when 10 mM of GSH was added, a large amount of NO quickly was released by HN@Cu-MOF (Fig. 4B and Fig. S3, ESI†). This phenomenon can be attributed to the presence of HN, which is an organic nitric ester-based NO donor that exhibits responsiveness towards GSH for NO release. Consequently, HN@Cu-MOF is extremely sensitive to GSH and can produce a large amount of NO.

3.3. Detection of $^{\bullet}$OH release

Then, methyl blue (MB) was applied to detect the emergence of $^{\bullet}$OH. MB has a strong absorption at 664 nm, but after reacting with $^{\bullet}$OH, its absorption at 664 nm decreases.[49] The previous experiments and research indicated that the HN shell largely prevents drug release from drug-loaded NPs.[26] Thus, HAase was applied in the $^{\bullet}$OH release experiment to degrade HN and release $^{\bullet}$OH. When MB was treated with H_2O_2 and H_2O_2 + HAase + HN@Cu-MOF, almost no changes were observed in the absorption of MB in comparison with pure MB solution under the same circumstances (Fig. 4C). However, the absorption declined greatly in the presence of MB, H_2O_2, HAase, HN@Cu-MOF and GSH, which demonstrated the considerable generation of $^{\bullet}$OH. With time, the absorption of MB at 664 nm declined gradually, suggesting the GSH-assisted Fenton-like reaction of HN@Cu-MOF.

3.4. Detection of $^1O_2$ release

To confirm the $^1O_2$ release due to Cu-MOF and HN@Cu-MOF under different conditions, the 1,3-diphenylisobenzofuran

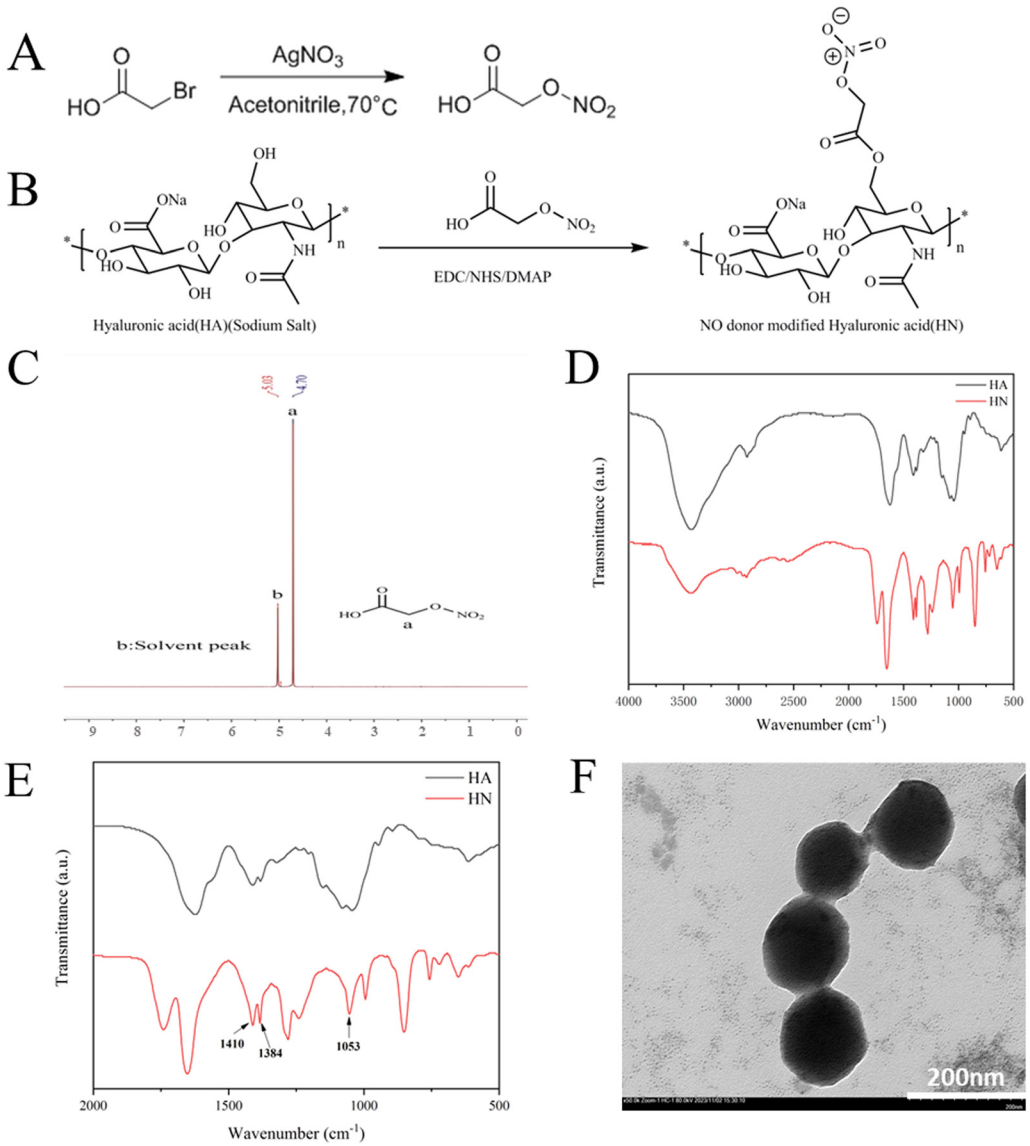

Fig. 2 The synthesis of 2-(nitrooxy)acetic acid (A) and HN (B). (C) The ^{1}H NMR spectrum of 2-(nitrooxy) acetic acid in D_2O. (D) The FTIR spectra of HA and HN. (E) The magnified FTIR spectra of HA and HN. (F) The TEM images of the HN@Cu-MOF.

(DPBF) assay was used. DPBF has a strong absorption at 417 nm, but once reacted with $^{1}O_2$ as a singlet oxygen scavenger, its absorption declines. To investigate the effect of Cu^{2+} doping on the ability to produce $^{1}O_2$, we compared the ability of the MOF and Cu-MOF to produce $^{1}O_2$ under laser irradiation. We added HAase to eliminate the impact of the HN shell on the $^{1}O_2$ release and set control groups with and without GSH to explore the effect of the high concentration of GSH in TEM on their $^{1}O_2$ production capacity. DPBF with or without laser showed no significant decrease (Fig. 5A). The absorbance of Cu-MOF showed a more significant decreased compared with the MOF due to the successful doping of Cu^{2+} (Fig. 5B and C), respectively. After the addition of GSH to each group, the rate of decrease was significantly reduced (Fig. 5B–D). We speculated that Cu^{2+} reacted with GSH to form Cu^{+}, together with consuming the part of GSH that reacts with $^{1}O_2$.

3.5. Cellular experiments with HN@Cu-MOF

Considering the above-mentioned tremendous therapeutic performance of HN@Cu-MOF, its anti-tumor effect was further researched on the cellular level using 4T1 cells (mouse breast cancer cells). Firstly, MTT assays were used to measure the biosafety of HN@Cu-MOF. Without irritation, as the concentration of Cu-MOF and HN@Cu-MOF increased, the cytotoxicity to 4T1 cells gradually increased. Also, HN@Cu-MOF was more toxic (Fig. 6A). At the concentration of 30 μg mL^{-1}, Cu-MOF exhibited a cell survival rate of 66%, while that of HN@Cu-MOF was 47%. This is due to the chemodynamic therapy (CDT) of Cu-MOF, which can kill 4T1 cells even without irritation. Due to the targeting of HN, the uptake of HN@Cu-MOF by 4T1 cells is greater than that of Cu-MOF. Therefore, HN@Cu-MOF was more cytotoxic to the 4T1 cells than Cu-MOF.

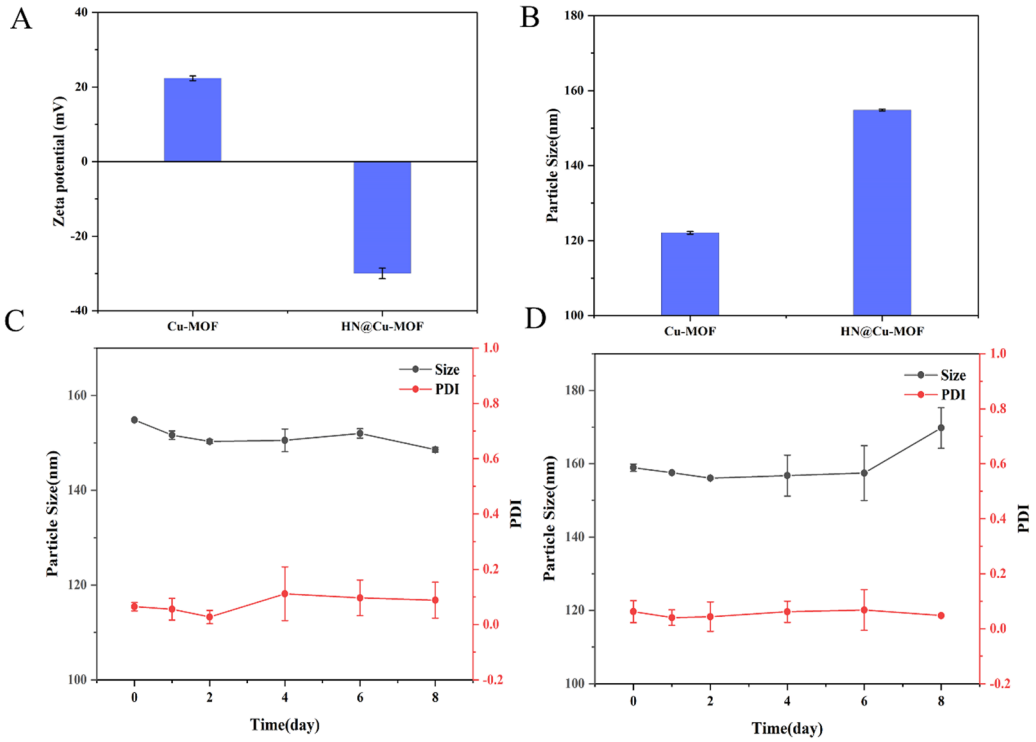

Fig. 3 The zeta potential (A) and particle size (B) of the Cu-MOF and HN@Cu-MOF (n = 3). The stability of the HN@Cu-MOF in (C) PBS 7.4 and (D) serum-containing culture medium (n = 3).

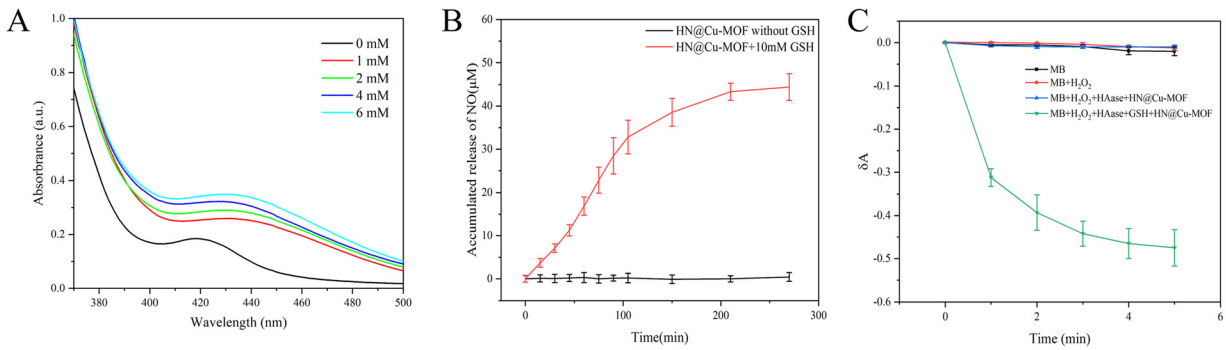

Fig. 4 (A) HN@Cu-MOF-mediated GSH consumption. (B) The accumulated release of NO from the HN@Cu-MOF with or without GSH. (C) The detection of •OH release of the HN@Cu-MOF.

Under 655 nm laser irradiation (50 mW cm^{-2}, 3 min), both Cu-MOF and HN@Cu-MOF exhibited stronger cytotoxic effects than that without irritation (Fig. 6B). At the concentration of 30 μg mL^{-1}, the cell survival rate of Cu-MOF was 32%, while that of HN@Cu-MOF was only 16%. Under irradiation from a 655 nm laser, HN@Cu-MOF showed the ability of photodynamic therapy, chemodynamic therapy and release of nitric oxide simultaneously and stronger cellular uptake.

To research the intracellular uptake of the MOF nanoparticles in 4T1 cells overexpressing CD44 receptors, CLSM was employed to evaluate the results qualitatively (Fig. 7A and B). The blue fluorescence showed the location of the cell nucleus labeled by DAPI, while red fluorescence was emitted by the photosensitizer TCPP, which represents the uptake performance of MOF by 4T1 cells. The red fluorescence intensity of MOF and Cu-MOF showed no significant difference. The uptake performance of MOF and Cu-MOF by the 4T1 cells was basically identical and the doping of Cu^{2+} did not affect it. Compared with MOF and Cu-MOF, HN@Cu-MOF showed stronger red fluorescence. Also, the cellular uptake of HN@Cu-MOF was significantly stronger than MOF and Cu-MOF, demonstrating that the surface modification of HN dramatically increased the uptake of the nanoparticles. The use of HN-pre-saturated CD44 receptors on the surface of 4T1 cells could significantly reduce the uptake of HN@Cu-MOF by cells,

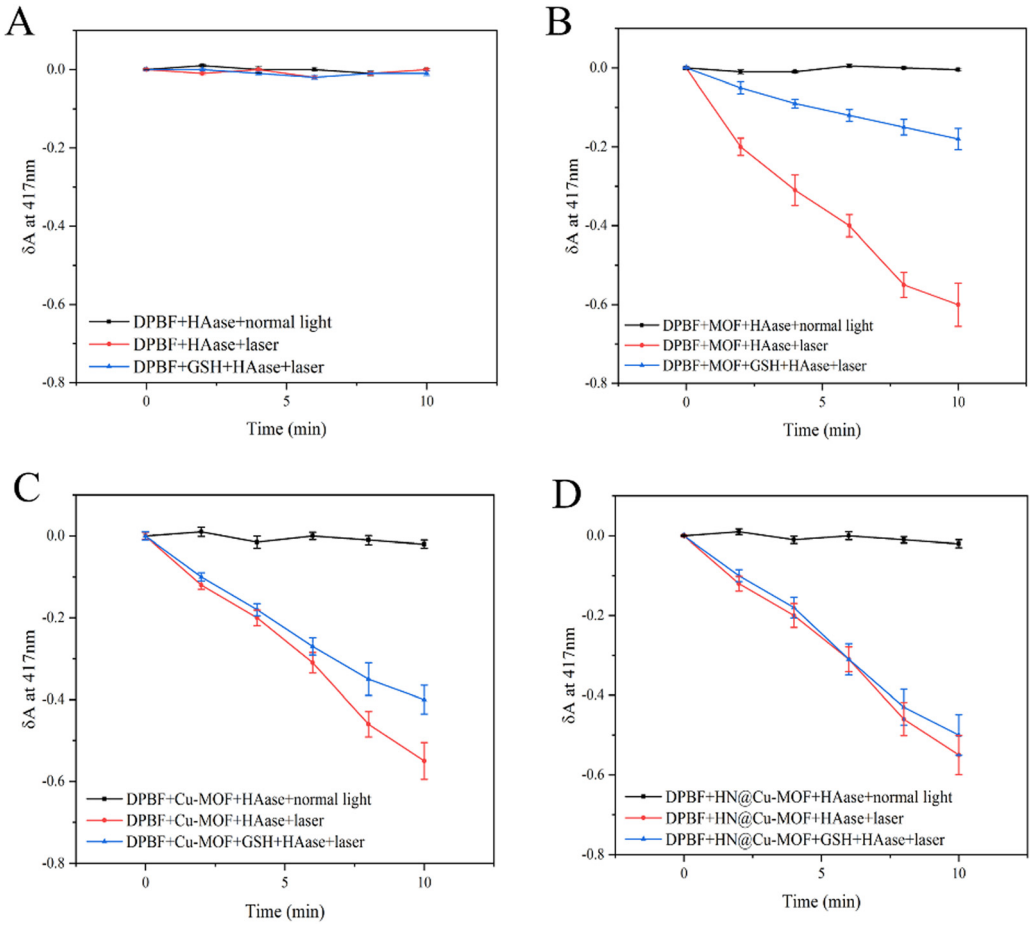

Fig. 5 (A) The detection of ROS release from DPBF. (B) The detection of ROS release from MOFs. (C) The detection of ROS release from Cu-MOFs. (D) The detection of ROS release from the HN@Cu-MOF.

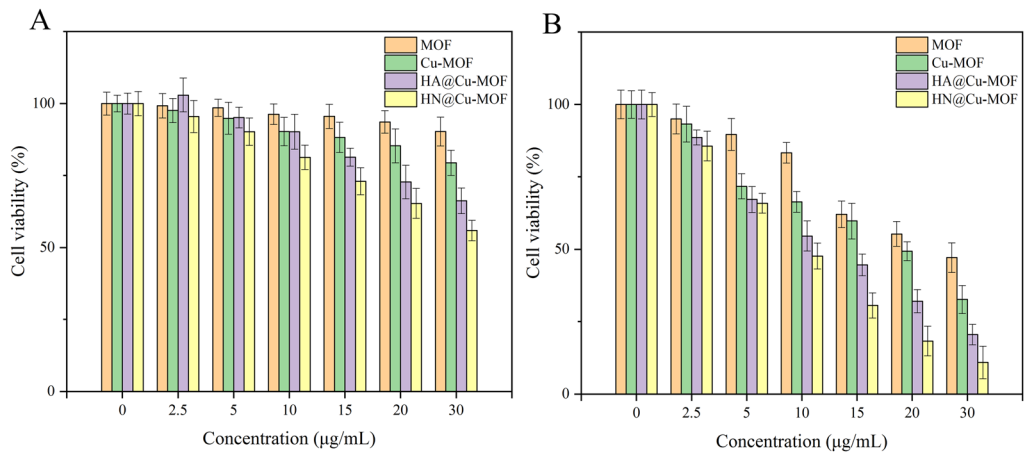

Fig. 6 The cell viability of 4T1 cells treated with the Cu-MOF and HN@Cu-MOF: (A) without irritation (B) with irritation.

which further proved the cellular uptake of HN@Cu-MOF through the CD44 receptor pathway.

The formation of singlet oxygen was further investigated, and the results are shown in Fig. 7C. Green fluorescence indicates the singlet oxygen ROS generated in the cells, which were labeled by DCFH-DA. Compared with TCPP, which has almost no fluorescence, the green fluorescence of MOF significantly increased. Furthermore, compared with MOF, the green

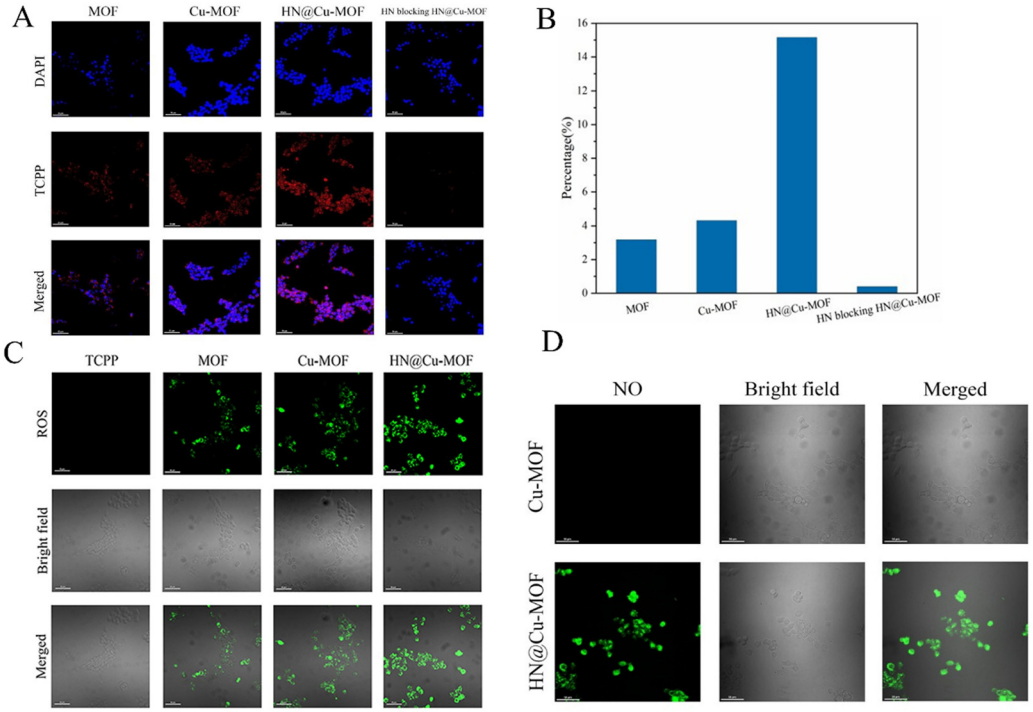

Fig. 7 (A) The CLSM images and (B) fluorescence intensity of 4T1 cells treated with TCPP, Cu-MOFs, the HN@Cu-MOF, and the HA blocking HN@Cu-MOF. (C) The fluorescence images of ROS in 4T1 cells treated with TCPP, MOFs, Cu-MOFs and the HN@Cu-MOF. (D) The fluorescence images of NO in 4T1 cells under irritation after treatment with Cu-MOFs and the HN@Cu-MOF.

fluorescence of Cu-MOF dramatically increased. The reason for this is that Cu^{2+} can consume GSH, which is overexpressed in tumor cells, and less ROS will be reduced. The green fluorescence of HN@Cu-MOF also increased, which is due to the increased cellular uptake caused by the targeting effect of HN. The above-mentioned results prove that Cu-MOF can increase the photodynamic effect by reducing the content of GSH in cells, and HN@Cu-MOF has the strongest ROS generation efficiency among the samples.

Then, we researched the NO-release property of HN@Cu-MOF in 4T1 cells by CLSM (Fig. 7D). DAF-FM-DA was used to label the NO produced in the cells and demonstrated green fluorescence. Cu-MOF did not show green fluorescence under laser irradiation, while HN@Cu-MOF demonstrated robust green fluorescence under the same conditions. This proved that HN could produce NO in tumor cells.

3.6. Biocompatibility and *in vivo* biodistribution

Red blood cells (RBCs) were incubated with HN@Cu-MOF for 4 h (Fig. 8A), which caused almost no hemolysis, demonstrating the hemocompatibility of HN@Cu-MOF for long-term circulation. Using *ex vivo* fluorescence to monitor the biodistribution behavior of Cu-MOF and HN@Cu-MOF. The heart, liver, spleen, lung, kidney and tumor of the mice were harvested and observed at 4, 8, 12, 24, and 48 h after injection of different drugs (Fig. 8B). After 4 h injection of Cu-MOF and HN@Cu-MOF, fluorescence signals were observed in the tumor tissue, and with time, the accumulation of Cu-MOF and HN@Cu-MOF in the tumor site gradually increased. At 12 h, the fluorescence intensity of Cu-MOF and HN@Cu-MOF at the tumor sites reached the maximum, and the fluorescence intensity of HN@Cu-MOF was stronger than that of Cu-MOF, which showed that compared with Cu-MOF, HN@Cu-MOF could be accumulated more in the tumor site. The reason for this is that the negatively charged HN modified on the surface of the nanoparticles could reduce the recognition and clearance of the nanoparticles and actively target the CD44 receptor of the cell membrane. Subsequently, the fluorescence intensity of Cu-MOF and HN@Cu-MOF at the tumor site began to weaken. Also, the fluorescence at the liver site began to increase, indicating that the drugs were metabolized in the liver.

3.7. *In vivo* anti-tumor efficacy

Based on the excellent anti-tumor effect *in vitro* and biodistribution *in vivo*, the *in vivo* anti-tumor effect of MOFs was examined on 4T1 tumor-bearing mice. The mice were randomly divided into five groups (saline, Cu-MOF, Cu-MOF with 655 nm laser, HN@Cu-MOF and HN@Cu-MOF with 655 nm laser) if the tumor volume reached about 100 mm^3. Additionally, every two days, the bodyweight and tumor volume of the mice in the different groups were noted.

The tumor growth photos and curves of the different preparation groups are shown in Fig. 9A and B, respectively. According to the growth of the tumor volumes over time in the tumor-bearing mice, the anti-tumor effects of the different

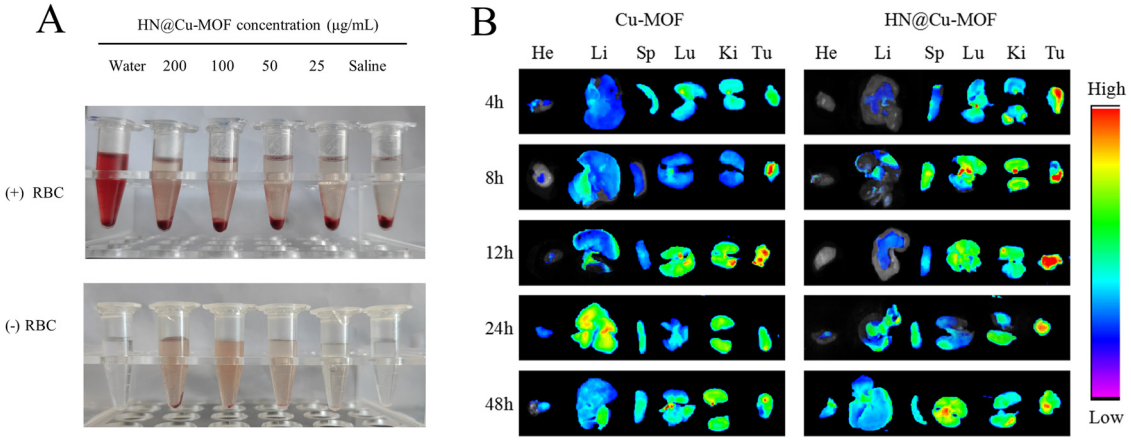

Fig. 8 (A) Hemolysis experiments with different concentrations of the HN@Cu-MOF. (B) The biodistribution of Cu-MOFs and the HN@Cu-MOF NPs in major organs and tumors at 4, 8, 12, 24, and 48 h post-injection.

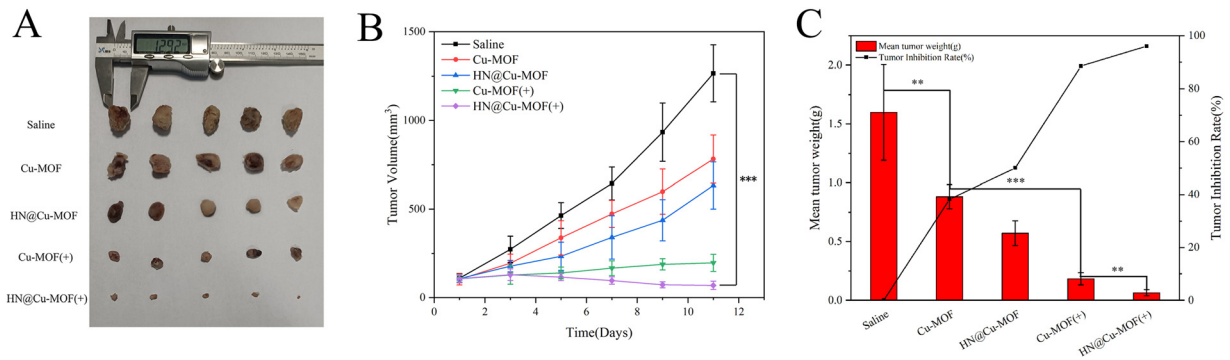

Fig. 9 (A) The photographs of the tumors from mice after different treatments. (B) Changes in tumor volume after the injection of different drugs. (C) The tumor weight and inhibition of mice after 11 days of different treatments (n = 5, *p < 0.05, **p < 0.01, and ***p < 0.001).

preparations were investigated. Compared with the saline group, the tumors of the other three groups of tumor-bearing mice grew slowly. It can be seen that the tumors of the HN@Cu-MOF(+) group (HN@Cu-MOF with laser) grew the slowest and were well inhibited. All the drug-administered groups showed a tumor-inhibiting effect. The average tumor volume in the saline group was 1200 mm^3 by the end of the experiment given that there was no tumor growth inhibition. In comparison, the tumor volume of the mice treated with Cu-MOF slightly declined compared with the saline group. This is due to the $^{\bullet}OH$ generated from the Fenton-like reaction. The tumor growth rate in the non-laser-irradiated groups (Cu-MOF and HN@Cu-MOF) was greater than that in the corresponding laser-irradiated group, which proved that the laser could excite TCPP in the composite nanoparticles, thereby generating singlet oxygen and inhibiting the growth of the tumor cells. Compared with Cu-MOF(+) (Cu-MOF with laser), HN@Cu-MOF(+) had a higher tumor suppression efficiency, which is mainly due to the increased stability in the plasma and long-term circulation. This was caused by the nitric oxide donor-modified hyaluronic acid on the surface of the HN@Cu-MOF. Simultaneously, HN@Cu-MOF had the capacity to actively target the CD44 receptors on the tumor cell membrane. It is worth noting from the body weight variations that except for the Cu-MOF(+) group, there no significant weight loss occurred in the other groups (Fig. S4, ESI†), implying that the lack of selectivity of the unencapsulated Cu-MOF led to the systemic distribution of Cu-MOF and produced greater toxic and side effects on most normal tissues. Furthermore, the photographs of the tumors, the tumor weight and the tumor inhibition rate together with the tumor growth curves provide additional evidence of the decreased tumor size following the various forms of treatment (Fig. 9).

H&E staining of the tumor tissues was employed to further prove the effectiveness of MOFs. The tumor from the HN@Cu-MOF with 655 nm laser irritation group showed the largest necrosis area among the groups (Fig. 10B). The major organs from the saline group and HN@Cu-MOF with laser irritation group were subjected to H&E staining for further safety analysis (Fig. 10A). All the H&E-stained organ tissue sections illustrated no obvious existence of pathological abnormalities. Thus, all the above-mentioned results suggest that HN@Cu-MOF had an excellent anti-tumor effect and no exhibited harm to normal tissues.

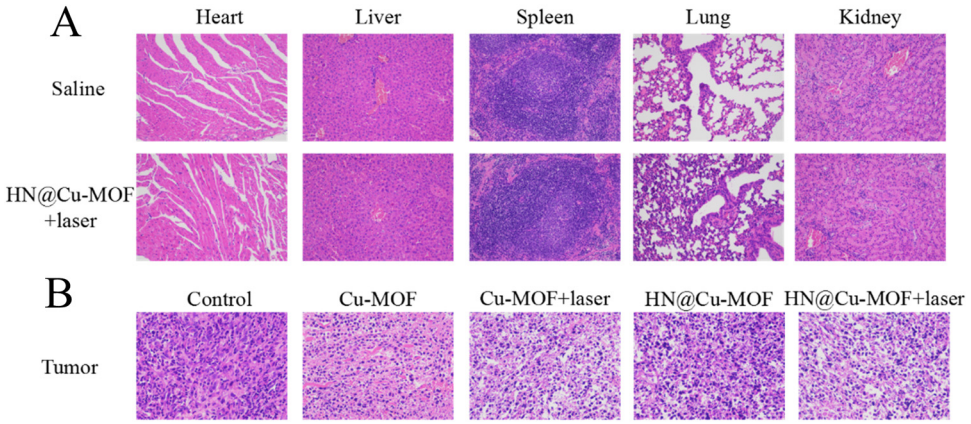

Fig. 10 (A) The H&E staining images of heart, liver, spleen, lung, and kidney obtained from the saline group and HN@Cu-MOF + laser group. (B) The H&E staining images of tumors in different treatment groups after the treatment. The scale bar is 100 μm.

4. Conclusions

In this study, we designed a smart therapeutic nanoplatform based on HN@Cu-MOF for combining PDT/CDT/GT. The Cu^{2+}-doped MOF consumed GSH and demonstrated the effect of CDT, enhancing the efficacy of both PDT and CDT simultaneously. Because of the existence of HN, HN@Cu-MOF possessed significant advantages in cellular uptake. Moreover, the combination of gas therapy, photodynamic therapy and chemodynamic therapy of HN@Cu-MOF effectively killed 4T1 cells and cured 4T1 tumor-bearing mice. The HN@Cu-MOF group showed the strongest tumor suppression among the groups on account of the CD44 receptor-mediated targeting and combination of three different types of therapy. The efficacy experiment results demonstrated that HN@Cu-MOF combines PDT/CDT/GT, maximizing the effectiveness of CDT/PDT and exerting a potent anti-tumor effect by consuming GSH and mitigating the hypoxic microenvironment. Overall, HN@Cu-MOF is a promising MOF for cancer treatment.

Conflicts of interest

The authors have no conflicts of interest to declare.

Acknowledgements

This work was supported by Shenyang Key Laboratory Project of Functional Drug Carrier Materials (Grant no. 19-110-4-08), 2020 Liaoning General Undergraduate Higher Education Inter-University Cooperation Program.

References

1 L. Cheng, C. Wang, L. Feng, K. Yang and Z. Liu, *Chem. Rev.*, 2014, **114**, 10869–10939.
2 D. Guo, S. Xu, Y. Huang, H. Jiang, W. Yasen, N. Wang, Y. Su, J. Qian, J. Li, C. Zhang and X. Zhu, *Biomaterials*, 2018, **177**, 67–77.
3 J. Hu, Y. a Tang, A. H. Elmenoufy, H. Xu, Z. Cheng and X. Yang, *Small*, 2015, **11**, 5860–5887.
4 X. Wang, J. Hu, P. Wang, S. Zhang, Y. Liu, W. Xiong and Q. Liu, *Theranostics*, 2015, **5**, 772–786.
5 Z. Zhou, J. Song, L. Nie and X. Chen, *Chem. Soc. Rev.*, 2016, **45**, 6597–6626.
6 C. Liu, Y. Cao, Y. Cheng, D. Wang, T. Xu, L. Su, X. Zhang and H. Dong, *Nat. Commun.*, 2020, **11**, 1735.
7 J. Zhang, N. Wang, Q. Li, Y. Zhou and Y. Luan, *Chem. Commun.*, 2021, **57**, 2305–2308.
8 W. Borzęcka, P. M. R. Pereira, R. Fernandes, T. Trindade, T. Torres and J. P. C. Tomé, *J. Mater. Chem. B*, 2022, **10**, 3248–3259.
9 J. J. Schuitmaker, P. Baas, H. L. L. M. van Leengoed, F. W. van der Meulen, W. M. Star and N. van Zandwijk, *J. Photochem. Photobiol., B*, 1996, **34**, 3–12.
10 J. I. Lee, T. G. Ahn and J. H. Choi, *J. Nippon Med. Sch.*, 2023, **90**, 41–49.
11 T. Minamide, Y. Yoda, K. Hori, K. Shinmura, Y. Oono, H. Ikematsu and T. Yano, *Surg. Endosc.*, 2020, **34**, 899–906.
12 R. Bonnett, *Chem. Soc. Rev.*, 1995, **24**, 19–33.
13 Y. Zhou, F. Tong, W. Gu, S. He, X. Yang, J. Li, Y.-D. Gao and H. Gao, *Acta Pharm. Sin. B*, 2022, **12**, 1416–1431.
14 F. Jiang, C. Yang, B. Ding, S. Liang, Y. Zhao, Z. Cheng, M. Liu, B. Xing, P. A. Ma and J. Lin, *Chin. Chem. Lett.*, 2022, **33**, 2959–2964.
15 L.-S. Lin, J. Song, L. Song, K. Ke, Y. Liu, Z. Zhou, Z. Shen, J. Li, Z. Yang, W. Tang, G. Niu, H.-H. Yang and X. Chen, *Angew. Chem., Int. Ed.*, 2018, **57**, 4902–4906.
16 P. Vaupel and A. Mayer, *Cancer Metastasis Rev.*, 2007, **26**, 225–239.
17 C. Liu, J. Wang, J. J. Wan and C. Z. Yu, *Coord. Chem. Rev.*, 2021, **432**, 213743.
18 M. Lismont, L. Dreesen and S. Wuttke, *Adv. Funct. Mater.*, 2017, **27**, 1606314.
19 S. R. Alves, I. R. Calori and A. C. Tedesco, *Mater. Sci. Eng., C*, 2021, **131**, 112514.

20 K. D. Lu, C. B. He, N. N. Guo, C. Chan, K. Y. Ni, R. R. Weichselbaum and W. B. Lin, *J. Am. Chem. Soc.*, 2016, **138**, 12502–12510.
21 X. Jiang, Y. Zhao, S. Sun, Y. Xiang, J. Yan, J. Wang and R. Pei, *J. Mater. Chem. B*, 2023, **11**, 6172–6200.
22 C. Ou, Y. Zhang, W. Ge, L. Zhong, Y. Huang, W. Si, W. Wang, Y. Zhao and X. Dong, *Chem. Commun.*, 2020, **56**, 6281–6284.
23 Z. Tang, Y. Liu, M. He and W. Bu, *Angew. Chem., Int. Ed.*, 2019, **58**, 946–956.
24 J. Y. Uriu-Adams and C. L. Keen, *Mol. Aspects Med.*, 2005, **26**, 268–298.
25 E. Brillas, M. A. Baños, S. Camps, C. Arias, P.-L. Cabot, J. A. Garrido and R. M. Rodríguez, *New J. Chem.*, 2004, **28**, 314–322.
26 J. Liang, W. Zhang, J. Wang, W. Li, F. Ge, W. Jin and Y. Tao, *ACS Omega*, 2023, **8**, 19402–19412.
27 L.-S. Lin, T. Huang, J. Song, X.-Y. Ou, Z. Wang, H. Deng, R. Tian, Y. Liu, J.-F. Wang, Y. Liu, G. Yu, Z. Zhou, S. Wang, G. Niu, H.-H. Yang and X. Chen, *J. Am. Chem. Soc.*, 2019, **141**, 9937–9945.
28 Y. Sun, X. Du, J. Liang, D. Wang, J. Zheng, Z. Bao, Z. Zhao and Y. Yuan, *J. Colloid Interface Sci.*, 2023, **645**, 607–617.
29 C. Zhang, L. Yan, X. Wang, X. Dong, R. Zhou, Z. Gu and Y. Zhao, *Nano Lett.*, 2019, **19**, 1749–1757.
30 Y. Zhong, Z. Peng, Y. Peng, B. Li, Y. Pan, Q. Ouyang, H. Sakiyama, M. Muddassir and J. Liu, *J. Mater. Chem. B*, 2023, **11**, 6335–6345.
31 Y. Deng, F. Jia, S. Chen, Z. Shen, Q. Jin, G. Fu and J. Ji, *Biomaterials*, 2018, **187**, 55–65.
32 J. Li, Y. Zhou, J. Liu, X. Yang, K. Zhang, L. Lei, H. Hu, H. Zhang, L. Ouyang and H. Gao, *J. Controlled Release*, 2022, **352**, 313–327.
33 X. Dong, H. J. Liu, H. Y. Feng, S. C. Yang, X. L. Liu, X. Lai, Q. Lu, J. F. Lovell, H. Z. Chen and C. Fang, *Nano Lett.*, 2019, **19**, 997–1008.
34 C. Hu, X. Cun, S. Ruan, R. Liu, W. Xiao, X. Yang, Y. Yang, C. Yang and H. Gao, *Biomaterials*, 2018, **168**, 64–75.
35 Z. X. Wang, A. L. Jin, Z. Yang and W. Huang, *ACS Nano*, 2023, **17**, 8935–8965.
36 M. Korbelik, C. S. Parkins, H. Shibuya, I. Cecic, M. R. Stratford and D. J. Chaplin, *Br. J. Cancer*, 2000, **82**, 1835–1843.
37 V. Rapozzi, E. D. Pietra and B. Bonavida, *Redox Biol.*, 2015, **6**, 311–317.
38 M. Xia, Y. Yan, H. Pu, X. Du, J. Liang, Y. Sun, J. Zheng and Y. Yuan, *Chem. Eng. J.*, 2022, **442**, 136295.
39 G. Honeth, P. O. Bendahl, M. Ringner, L. H. Saal, S. K. Gruvberger-Saal, K. Lovgren, D. Grabau, M. Ferno, A. Borg and C. Hegardt, *Breast Cancer Res.*, 2008, **10**, R53.
40 C. Y. Wang, C. S. Huang, Y. P. Yang, C. Y. Liu, Y. Y. Liu, W. W. Wu, K. H. Lu, K. H. Chen, Y. L. Chang, S. D. Lee and H. C. Lin, *J. Chin. Med. Assoc.*, 2019, **82**, 196–201.
41 R. Asai, H. Tsuchiya, M. Amisaki, K. Makimoto, A. Takenaga, T. Sakabe, S. Hoi, S. Koyama and G. Shiota, *Cancer Med.*, 2019, **8**, 773–782.
42 A. Bartolazzi, R. Peach, A. Aruffo and I. Stamenkovic, *J. Exp. Med.*, 1994, **180**, 53–66.
43 H. Xu, M. Niu, X. Yuan, K. Wu and A. Liu, *Exp. Hematol. Oncol.*, 2020, **9**, 36.
44 E. Bartheldyová, R. Effenberg, J. Mašek, L. Procházka, P. T. Knötigová, P. Kulich, F. Hubatka, K. Velínská, J. Zelníčková, D. Zouharová, M. Fojtíková, D. Hrebík, P. Plevka, R. Mikulík, A. D. Miller, S. Macaulay, D. Zyka, L. Drož, M. Raška, M. Ledvina and J. Turánek, *Bioconjugate Chem.*, 2018, **29**, 2343–2356.
45 Y. Han, S. Gao, Y. Zhang, Q. Ni, Z. Li, X. J. Liang and J. Zhang, *Bioconjugate Chem.*, 2020, **31**, 1247–1258.
46 J. Hu, W. Wu, Y. Qin, C. Liu, P. Wei, J. Hu, P. H. Seeberger and J. Yin, *Adv. Funct. Mater.*, 2020, **30**, 1910084.
47 D. Han, Y. Han, J. Li, X. Liu, K. W. K. Yeung, Y. Zheng, Z. Cui, X. Yang, Y. Liang, Z. Li, S. Zhu, X. Yuan, X. Feng, C. Yang and S. Wu, *Appl. Catal., B*, 2020, **261**, 118248.
48 W. Tan, T. Wei, J. Huo, M. Loubidi, T. Liu, Y. Liang and L. Deng, *ACS Appl. Mater. Interfaces*, 2019, **11**, 36782–36788.
49 Z. Xie, S. Liang, X. Cai, B. Ding, S. Huang, Z. Hou, P. Ma, Z. Cheng and J. Lin, *ACS Appl. Mater. Interfaces*, 2019, **11**, 31671–31680.